

Triboelectric nanogenerator embedded cylindrical roller bearing for rotational energy harvesting and self-powered fault diagnosis

Yida Xin^{a,b}, Taili Du^{a,*}, Ting Liu^b, Peiting Sun^a, Meixian Zhu^a, Lin Zheng^b, Haiying Du^b, Yongjiu Zou^a, Minyi Xu^{a,*}

^a Dalian Key Laboratory of Marine Micro/Nano Energy and Self-powered Systems, Marine Engineering College, Dalian Maritime University, Dalian 116026, China

^b College of Mechanical and Electronic Engineering, Dalian Minzu University, Dalian 116600, China

ARTICLE INFO

Keywords:
Triboelectric nanogenerator
Self-powered
Fault diagnosis
Smart bearing

ABSTRACT

Ensuring the normal operation of bearings is crucial for the safety of the equipment. In order to better monitor the condition of bearings, a smart triboelectric nanogenerator embedded cylindrical roller bearing (TCRB) is proposed. Its cylindrical rollers are made of polyetheretherketone (PEEK), and the outer ring consists of grid electrodes coated with nylon film. The present TCRB is demonstrated to achieve long-term stable operation. Experimentally, the TCRB can deliver a maximum output with an open-circuit voltage of 26.56 V and a short-circuit current of 2.45 μ A at 600 rpm, and the generated electricity is sufficient to drive small sensors. Moreover, the output can also be processed to realize the self-powered monitoring of the rotational speed with an error of less than 2%. Lastly, four distinct classification methods are utilized to diagnose typical bearing faults using the triboelectric signal, and the diagnostic method with both high levels of accuracy and robustness is determined. This study demonstrates the excellent performance of the TCRB in self-powering, self-sensing and self-diagnosing, providing a viable solution for the development of smart bearings.

1. Introduction

The rolling bearing is an important component for modern rotating machinery equipment. Its primary function is to support the rotating mechanical body and reduce the friction coefficient. The reliability of bearings is crucial for the stable operation of equipment. Therefore, real-time monitoring on the operating conditions of rolling bearings is an important means to avoid severe consequences resulting from rolling bearing malfunctions [1,2]. The monitoring of bearings mainly relies on temperature or vibration sensors mounted in or near the bearing seat. The installation of sensors is cumbersome and the measured signal is susceptible to being disturbed due to its distance from the bearing [3]. Moreover, most monitoring sensors are powered by batteries or cables. However, batteries need to be manually replaced regularly, and wiring is difficult to implement in confined spaces [4]. In recent years, the emergence of smart bearings offers a good choice for addressing these issues. By integrating monitoring sensors into the bearing structure, the smart bearing is expected to solve the complex sensor installation work on site. With the advancement of energy harvesting technology and signal processing technology, the smart bearing with multiple functions

of self-sensing, self-powering and self-diagnosing has been developed [5, 6]. It can facilitate the transfer of complex tasks, such as signal acquisition, sensor installation and power supply, from the user end to the production end, offering great convenience to clients [3]. Therefore, the study of smart bearings has attracted the interest of numerous researchers [7]. Holm et al. [6] developed a bearing with the self-diagnosing function by integrating multiple sensors and signal processing systems into the bearing. Gong et al. [8] proposed a variable reluctance energy harvester (VREH) that integrated with the existing structure of bearings to accomplish the self-powering function. Zhang et al. [9] designed a self-powered bearing that could collect rotational energy based on electromagnetic technology. Nevertheless, these attempts made substantial modifications to bearings, and their structural designs were not compact. Smart bearings with more compact structure need to be proposed.

Triboelectric nanogenerator (TENG) is a new power generation method based on Maxwell's displacement current principle. Since it was first proposed by Zhonglin Wang in 2012 [10], numerous researchers have affirmed its capability to collect diverse forms of energy [11,12], including wave energy [13,14], wind energy [15] and vibration energy

* Corresponding authors.

E-mail addresses: dutaili@dlmu.edu.cn (T. Du), xuminyi@dlmu.edu.cn (M. Xu).

[16–18]. Moreover, numerous researchers have effectively developed self-powered sensors based on TENG [19,20], including pressure sensors [21,22], vibration acceleration sensors [23,24] and tactile sensors [25–27]. In comparison to traditional power generation techniques, TENGs offer a variety of material options, simple structures and low manufacturing costs, thereby providing an alternative method for achieving the self-powering and self-sensing function of smart bearings. Meng et al. [28] developed an innovative self-powered bearing-structured speed sensor. Xie et al. [29] successfully designed a self-powered bearing that could measure the skidding rate of the bearing, and extended the service life of TENG-based bearings effectively by installing a sweeping charge supplement device. Jiang et al. [30] designed a compact self-powered bearing by coating PTFE on the wave cage and adding grid electrodes to the end cover, and successfully utilized its electric signal to diagnose typical bearing faults. So far, the majority of TENG-based bearings reported [28–32] have been modified based on the structure of the deep groove ball bearing. The cylindrical roller bearing is also a common type of bearing, possessing a better capacity for bearing loads and a larger contact area for triboelectric generation, but less research has been devoted to the development of TENG-based cylindrical roller bearings.

To address the above problems, this study presents the design of a triboelectric nanogenerator embedded cylindrical roller bearing (TCRB) with self-powering, self-sensing and self-diagnosing capabilities. The influences of speed, material selection, electrode width and other factors on the output performance are systematically analyzed. Besides, the speed monitoring through the processing of the electric output is specifically demonstrated. Furthermore, an in-depth research is conducted regarding the utilization of triboelectric signals for fault diagnosis. A new experiment based data partitioning method is proposed to address the issue of triboelectric signals being susceptible to environmental interference by varying the distribution of training and test sets. The performances of four distinct classification methods applied to fault diagnosis of the TCRB are investigated, and the classification method with high diagnostic accuracy and good robustness is determined.

2. Experimental section

The main dimensional parameters of the TCRB are illustrated in Table S1. The outer ring, inner ring and cage were all manufactured by SLA 3D printing technology. Polytetrafluoroethylene (PTFE), glass fibre reinforced polytetrafluoroethylene (GF-PTFE), polyoxymethylene (POM), and polyetherketone (PEEK) cylindrical rollers were purchased and fabricated from the Taobao Juanjuan Plastic Shop. There were small notches at the top of the outer ring for the convenience of electrodes leads extraction. Grid electrodes, with a copper thickness of 0.035 mm and a plate thickness of 0.13 mm, were produced by Shenzhen Huaxin Fast Circuit Factory. They had 8 pairs of staggered electrodes with a width of 11.5 mm. The 0.05-mm-thick polyimide film was acquired from the Taobao Goldfinger Store, while the nylon film with equivalent thickness was obtained from Lambert Optoelectronics. The polyimide film was used to cover the electrodes as an adhesive, followed by the attachment of the nylon film.

A servo motor with a maximum adjustable speed of 3000 rpm was selected in this experiment. Two aluminium alloy bearing seats were used to fix the shaft on the test rig, with the TCRB being positioned in the bearing seat far from the motor. The output of the TCRB was measured by a programmable electrometer (Keithley Model 6514) through a data acquisition system (NI PCI-6220, Texas, USA) and visualized through a program developed by LabVIEW (National Instruments, Austin, Texas, USA).

3. Result and discussion

3.1. Structure and working principle

Fig. 1 depicts the structural design of the TCRB, which can be used in a variety of devices, such as industrial robots and small-scale wind power generations, as illustrated in **Fig. 1a**. The TCRB consists of an inner ring, an outer ring, a basket-type cage, eight cylindrical rollers, a nylon film and grid electrodes, as illustrated in **Fig. 1b**. The number of grid electrodes is consistent with that of cylindrical rollers, and their length is equal to the circumference of the outer ring, as illustrated in **Fig. 1c**. The grid electrodes are closely affixed to the outer ring, and then covered with Kapton tape as the paste layer and nylon film as the contact layer. **Fig. 1d** presents a photograph of the cage and PEEK cylindrical rollers, while a fully assembled TCRB is illustrated in **Fig. 1e**.

The working principle of the TCRB is explained in **Fig. 2**. As the inner ring of the TCRB rotates in conjunction with the shaft, the cage and PEEK cylindrical rollers rotate at a certain speed with respect to the fixed electrodes. **Fig. S1** displays the force diagram of the outer ring, revealing that the cylindrical rollers make contact with the lower semicircle of the outer ring. The working principle of the TCRB can be elucidated as depicted in **Fig. 2a**. Due to the difference in electronegativity of nylon and PEEK, the nylon film is positively charged, whereas the PEEK rollers are negatively charged upon contact. When the PEEK rollers completely overlap electrode A (**Fig. 2a (i)**), electrode A becomes positively charged to screen the negative charges of the PEEK rollers. At this time, the maximum potential difference is attained between electrode A and electrode B. As the PEEK rollers rotate in the counterclockwise direction (**Fig. 2a (ii)**), electrons begin to transfer from electrode B to electrode A under the action of electrostatic balance, forming a current through the external circuit. When the PEEK rollers completely overlap electrode B (**Fig. 2a (iii)**), the potential difference between electrode A and electrode B is reversed to the maximum. As rollers continue to rotate (**Fig. 2a (iv)**), the potential difference between two electrodes leads to an opposite current flow. These four states are repeated with the operation of the TCRB, generating alternating current through the external circuit.

The potential distributions of the TCRB can be understood by conducting a finite element analysis using COMSOL software, as illustrated in **Fig. 2b**. The size of the model is consistent with the designed device. When PEEK rollers completely overlap the electrodes, the potential difference between the two electrodes achieves the maximum. When PEEK rollers are positioned between the two electrodes, there is no potential difference between the two electrodes.

3.2. Output performance of the TCRB

To acquire the output signal plainly and precisely, a bandstop filter is added to the LabVIEW-based measurement program to eliminate the 50 Hz power frequency interference of the motor. As illustrated in **Fig. S2**, the filtered signal can reflect the output of the TCRB in an intuitive manner. Cylindrical rollers are the primary load-bearing component and also have a substantial impact on triboelectrification. On the premise of ensuring the mechanical strength of the bearing, materials with wide operating temperature range and strong electronegativity should be selected. In this experiment, TCRBs with cylindrical rollers manufactured from four distinct engineering plastics are utilized, including PEEK, POM, GF-PTFE, and PTFE. As illustrated in **Fig. 3a**, the difference in the electric output between TCRBs with distinct cylindrical rollers is insignificant. The output voltage of the TCRB with POM rollers is the largest, while the output with PEEK rollers is comparable to that with PTFE-GF rollers. The main properties of the four materials are illustrated in Table S2, and it can be found that PEEK exhibits excellent performance in terms of both working temperature and strength. Therefore, PEEK is selected as the material for fabricating cylindrical rollers after considering the mechanical strength, electronegativity and working temperature range synthetically. The material selection of the

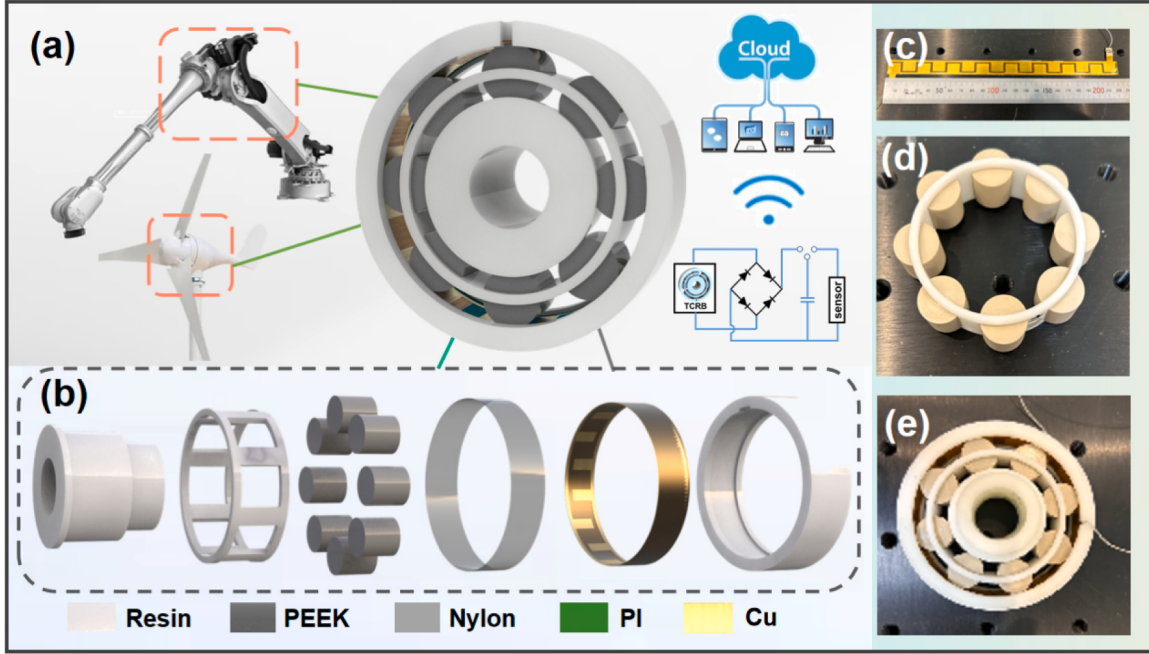


Fig. 1. Structural design of the TCRB. (a) Schematic illustration of various applications of the TCRB. (b) Components of the designed TCRB. (c) Photograph of the grid electrodes, (d) cage and cylindrical rollers, and (e) an assembled TCRB.

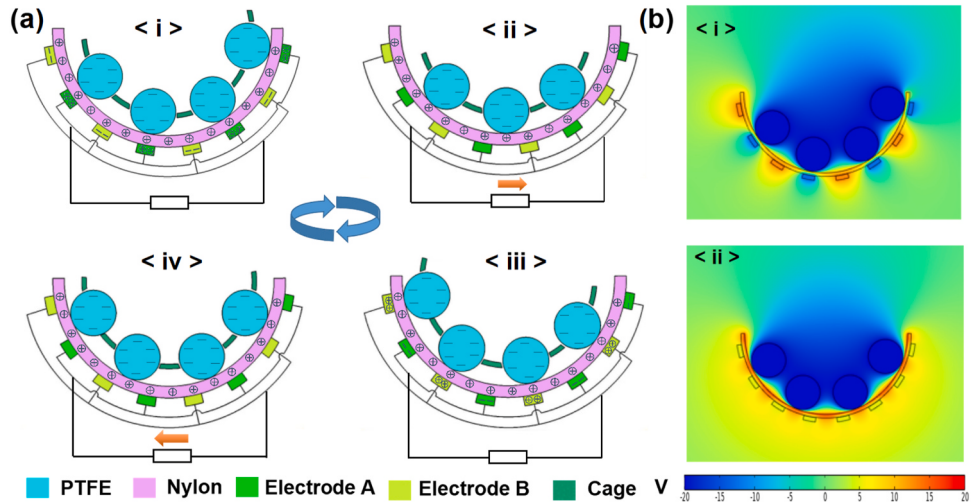


Fig. 2. Working principle of the TCRB. (a) Schematic illustration of the working principle of the TCRB. (b) Electric potential distributions at different positions.

thin film on the outer ring also has a significant impact on the electric output. The output performances of TCRBs with nylon, FEP and Kapton films are measured to determine the selection of film material. As illustrated in Fig. 3b, the TCRB with nylon film exhibits the optimal output performance, whereas the TCRB with Kapton film exhibits the worst output performance. Therefore, nylon is chosen as the film material on the outer ring in this work.

With the material selections of the TCRB determined, the relationship between electric outputs and speed is investigated. As illustrated in Figs. 3c and 3d, the output voltage and transferred charge of the device increase slowly with speed. This phenomenon can be attributed to the elevation of triboelectric charge density resulting from the escalating centrifugal force acting upon the rollers [33]. It is widely recognized that the current, denoted as I , can be mathematically represented as the derivative of charge with respect to time, dq/dt . The rapid increase in current with speed can be observed in Fig. 3e, which is attributed to

faster variation in dt over time compared to dq . Furthermore, when the rotational speed surpasses 1000 rpm, the device's output becomes unstable, which may be due to the poor machining precision of cylindrical rollers and the inner ring, as well as the protrusion of the copper part on grid electrodes. Fig. 3f presents the output of the TCRB with various electrode widths. It indicates that increasing the width of grid electrodes can greatly improve the TCRB's output performance, which is due to that wider electrode width leads to the contact between dielectrics and electrodes more synchronously.

Metal bearings, in traditional practice, require the addition of lubricating oil or grease to mitigate friction during operation. However, the addition of grease reduces the output of the device significantly, as illustrated in Fig. 3g, which is due to that the lubricating grease suppresses the amount of triboelectric charge. Hence, lubricating grease should be avoided to ensure the output performance of the TCRB. The cylindrical rollers and outer ring film of the TCRB in this case are made

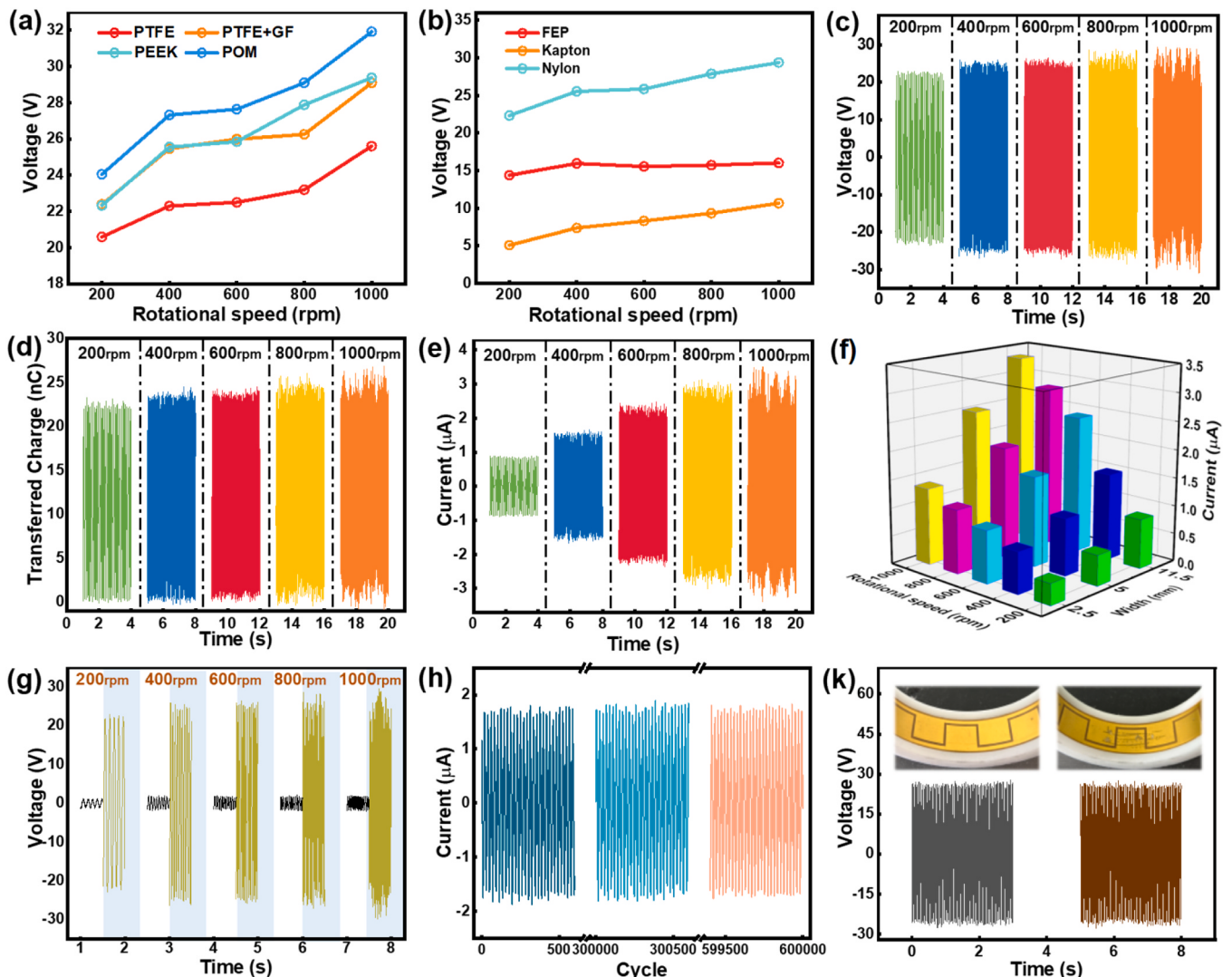


Fig. 3. Output performance of the TCRB. (a) Output performance of the TCRBs with different roller materials. (b) Output performance of the TCRBs with different film materials. (c) Output voltage, (d) transferred charge, and (e) current of the TCRB at different rotational speeds. (f) Electric output of the TCRB with different electrode widths. (g) The influence of lubricating grease on the output performance. (h) Continuous electric output of the TCRB. (k) Schematic illustration of the robust electric output.

of a pair of engineering plastic materials with self-lubrication property and notable difference in electronegativity, enabling the TCRB to achieve high electric output without lubricating medium. At 600 rpm, the TCRB can achieve an electric output of 26.56 V and 2.45 μ A, exhibiting better output performance compared to similarly sized TENG-based spherical roller bearings [28–32]. A reliability assessment of the TCRB was performed through a 600,000 cycles operation test at 400 rpm. As illustrated in Fig. 3h, there is no significant change in the output of the device. Besides, the metallographic observations of nylon films operating for 2 h and 25 h without the addition of lubricating grease are illustrated in Fig. S3, and no evident scratches are found on the film surface. It is worth noting that the device can still maintain stable output even in the case where the outer nylon film is severely scratched, as illustrated in Fig. 3k. With the rapid advancement of material technology, new engineering plastic materials with better mechanical and self-lubrication properties are emerging constantly, such as fibre-enhanced PEEK [34], providing the possibility for better applications of TCRBs in the future.

3.3. Self-powering and self-sensing capability of the TCRB

Fig. 4a presents the photograph of the test rig. The self-powering capability of the TCRB was verified by experiments. As illustrated in Fig. 4b, the TCRB can achieve a peak instantaneous power of 38.4 μ W at 600 rpm under a load resistance of 30 M Ω . The insert in Fig. 4b shows that the device can light up 10 LEDs directly. Besides, the performance of the TCRB to charge capacitors through the rectifiers was also tested. As illustrated in Fig. 4c, a set of 10 μ F, 33 μ F and 100 μ F capacitors are charged through rectifier bridges from 0 to 3 V at 600 rpm, which take 35 s, 94 s and 471 s, respectively. The charged 100 μ F capacitor can drive the temperature and humidity sensor for more than 10 s, and the relevant demonstration can be found in the inset of Fig. 4c and Video S1.

Supplementary material related to this article can be found online at doi:10.1016/j.sna.2023.114664.

The speed sensing of the TCRB is achieved by analyzing the motion relationship of bearing parts and calculating the frequency of output signals. The outer ring remains fixed during the operation of the TCRB. Therefore, the rotating frequency of the bearing can be expressed as Eq. (1) under the assumption that there exists no sliding between each part

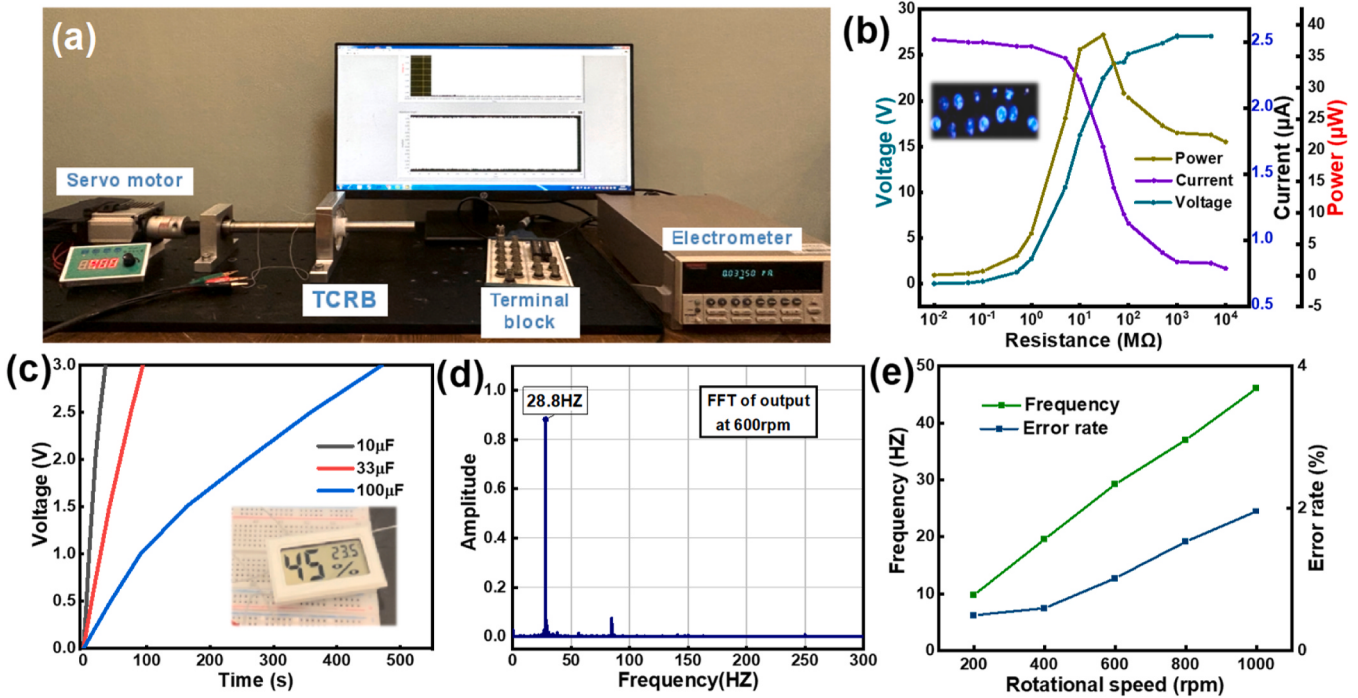


Fig. 4. Demonstration of the self-powering and self-sensing ability. (a) Photograph of the test rig. (b) Output voltage, current and power of the TCRB with external resistance loads. (c) Charging curve of different capacitors powered by the TCRB. (d) FFT spectrum of the output at 600 rpm. (e) Dependency of the output frequency and the error of speed sensing on the rotational speed.

of the rolling bearing [35].

$$f_{cage} = \frac{f_{rotor}}{2} \left(1 - \frac{d}{D} \cos\alpha \right) \quad (1)$$

where d is the diameter of the cylindrical roller; D is the pitch diameter of the roller bearing, that is, the diameter of the circle where the centre of the roller is located; α is the pressure angle of the bearing, and the pressure angle of the cylindrical roller bearing is 0° . The number of rollers and electrodes of the TCRB is denoted as N . According to the working principle of the TCRB, rollers and electrodes contact and separate N times for each revolution of the cage. Therefore, the output frequency of the TCRB (f_o) can be expressed as Eq. (2), and then the frequency of the rotor can be expressed as Eq. (3).

$$f_o = N f_{cage} \quad (2)$$

$$f_{rotor} = \frac{2f_o D}{N(D - d \cos\alpha)} \quad (3)$$

In this experiment, given that d is 15 mm, D is 55 mm and $N= 8$, so the rotational speed of the rotor can be calculated as follows:

$$\omega_{rotor} = 60f_{rotor} = 20.625\omega_o \quad (4)$$

According to Eq. (4), the speed is linearly related to the output frequency of the TCRB. The frequency of the electric output f_o can be derived by fast Fourier transform on the output, as illustrated in Fig. 4d. Then, a real-time speed monitoring system through processing output signal was developed in LabView, showing good performance in speed sensing, as can be seen in Video S2. As illustrated in Fig. 4e, the linear relationship between the actual measured speed and the TCRB output frequency is consistent with Eq. (4). However, it is worth noting that as the speed increases, there will be errors in the speed derived from the electric output, with a value of less than 2% within 1000 rpm. The gradual increase in error with speed may be due to the skidding issue caused by insufficient machining accuracy.

Supplementary material related to this article can be found online at

[doi:10.1016/j.sna.2023.114664](https://doi.org/10.1016/j.sna.2023.114664).

3.4. Application of the TCRB in fault diagnosis

As illustrated in Fig. 5a, we tested the output of the TCRB for four typical forms: fault-free, cage fault (CF), inner ring fault (IRF), and outer ring fault (ORF) at 400 rpm and 600 rpm with a sampling frequency of 2 kHz. The signals of various faults were acquired by replacing artificially made faulty parts.

For bearings with various faults, there will be the corresponding fault characteristic frequency on the frequency spectrum. Specifically, the characteristic frequencies corresponding to the TCRB with various faults can be expressed as follows [35,36].

$$f_{CF} = \frac{N}{2} f_{rotor} \left(1 - \frac{d}{D} \cos\alpha \right) \quad (5)$$

$$f_{IRF} = \frac{N}{2} f_{rotor} \left(1 + \frac{d}{D} \cos\alpha \right) \quad (6)$$

$$f_{ORF} = \frac{N}{2} f_{rotor} \left(1 - \frac{d}{D} \cos\alpha \right) \quad (7)$$

Subsequently, the frequency spectrum analysis is attempted for fault diagnosis. Fig. S4 presents the frequency spectrum diagrams corresponding to various faults at 600 rpm. However, due to the coincidence of f_{CF} and f_{ORF} with the output frequency (Eq. (2)), it is difficult to identify the fault characteristic frequency from the frequency spectrum intuitively. For the TCRB with inner ring fault, since the triboelectric output originates from the contact between the outer ring and the rollers, f_{IRF} is not readily apparent from the spectrum.

As a result, artificial intelligence (AI) based classification methods, including machine learning algorithms and deep learning algorithms, are employed instead for fault diagnosis. The preprocessing of the electric output is as follows. The test duration is set to 300 s once and the sample length is determined to be 3000, as illustrated in Fig. 5b. Given that the amplitude of TENG outputs is susceptible to interference such as

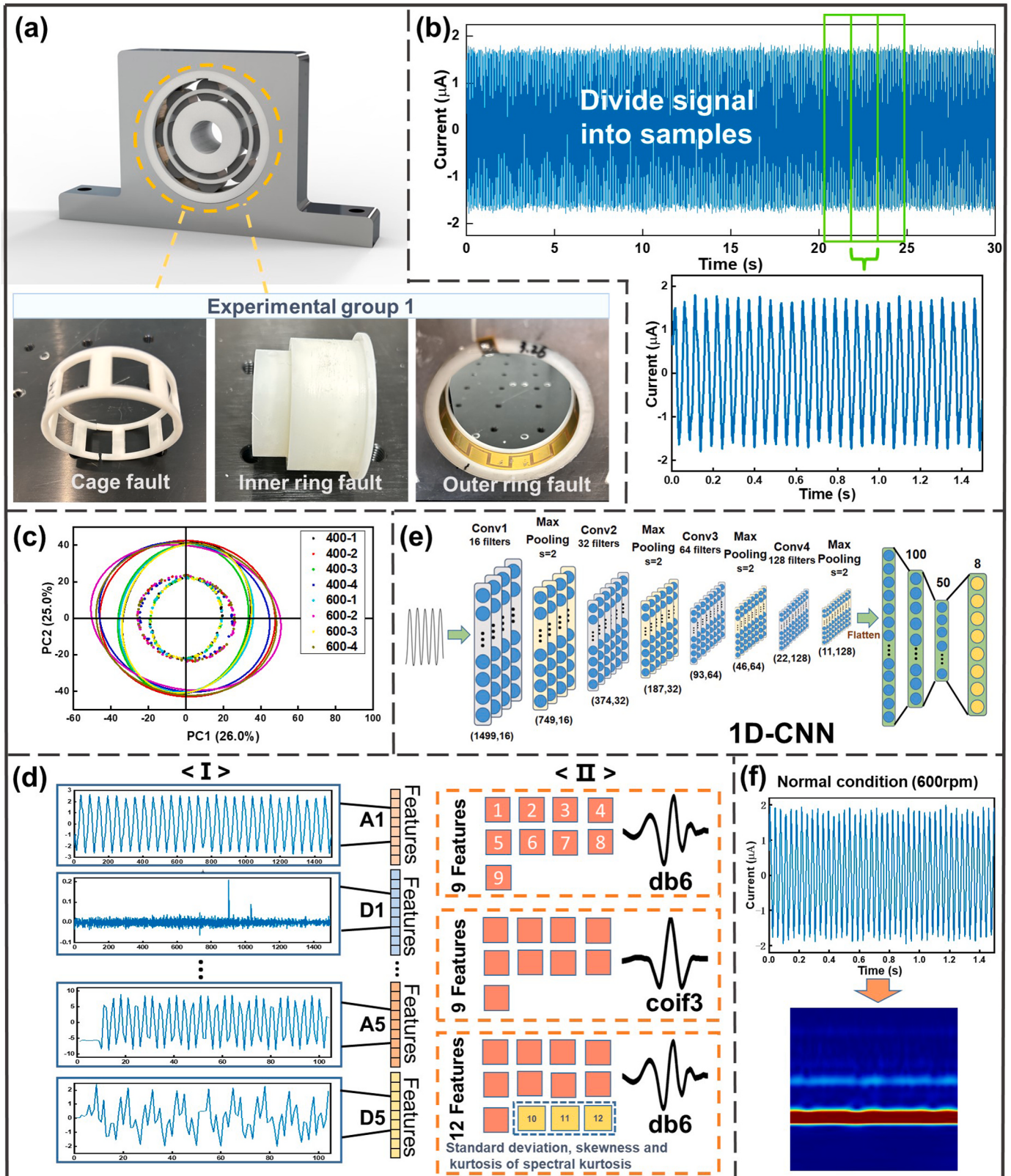


Fig. 5. Fault diagnosis of the TCRB. (a) Photographs of typical faults: cage fault, inner ring fault and outer ring fault. (b) Preprocessing of the electric output. (c) Schematic illustration of the two-dimensional PCA chart. (d) The feature extraction procedure of the DWT-XGBoost method. (e) Structure of the 1D-CNN model. (f) Schematic illustration of the image obtained through CWT.

humidity [37], a method for sample normalization is proposed. The normalization method is to make the average absolute value of the sample equal to one by multiplying a coefficient. Table S3 illustrates the structure of the entire partitioned dataset. It can be viewed that 200 samples are obtainable for each category. Then, the training set and the test set are obtained by randomly splitting samples at a ratio of 7:3.

In this study, machine learning based methods include principal component analysis (PCA)-eXtreme Gradient Boosting (XGBoost) and discrete wavelet transform (DWT)-XGBoost. For the PCA-XGBoost method, principal component analysis is first conducted on outputs of various categories to acquire features. Fig. 5c presents the schematic illustration of the first two principal components of the output. XGBoost algorithm, proposed by Chen Tianqi in 2016 [38], is chosen as the machine learning classifier due to the model's simplicity and excellent performance in classification accuracy. The optimal hyperparameters of XGBoost are determined using the grid search and 4-fold cross-validation method in Python. The classification accuracy of the PCA-XGBoost model is 87.71% when employing the first 50 principal components and 91.25% when employing the first 100 principal components. For the DWT-XGBoost method, the feature extraction technique adopts the discrete wavelet transform's time-frequency analysis

approach, as illustrated in Fig. 5d. Using Daubechies wavelet basis, five high-frequency components and five low-frequency components are acquired through discrete wavelet transform of the sample, and then nine time-frequency domain features are extracted from these components. As a result, a total of $10 \times 9 = 90$ features can be obtained from each sample. The set of nine extracted features contains waveform factor, crest factor, clearance factor, impulse factor, kurtosis, skewness, gravity frequency, mean square frequency and frequency variance. Detailed calculation formulas of these features implemented in Matlab can be seen in Table S4. The DWT-XGBoost method can achieve a classification accuracy of 99.17%.

Subsequently, two deep learning based methods are employed, including one-dimensional convolutional neural network (1D-CNN) and continuous wavelet transform (CWT)-Residual Network50 (ResNet50). The structure of the 1D-CNN model is plotted in Fig. 5e. It comprises convolution layers, maxpooling layers and fully connected layers, with rectified linear unit (RELU) as the activation function. The length and stride of the convolutional kernel are 3 and 2, while the maxpooling size is 2. 1D-CNN model exhibits a classification accuracy of 83.75%. Lastly, the CWT-ResNet50 method is adopted. Images with a size of $224 \times 224 \times 3$ corresponding to the samples are first obtained through continuous

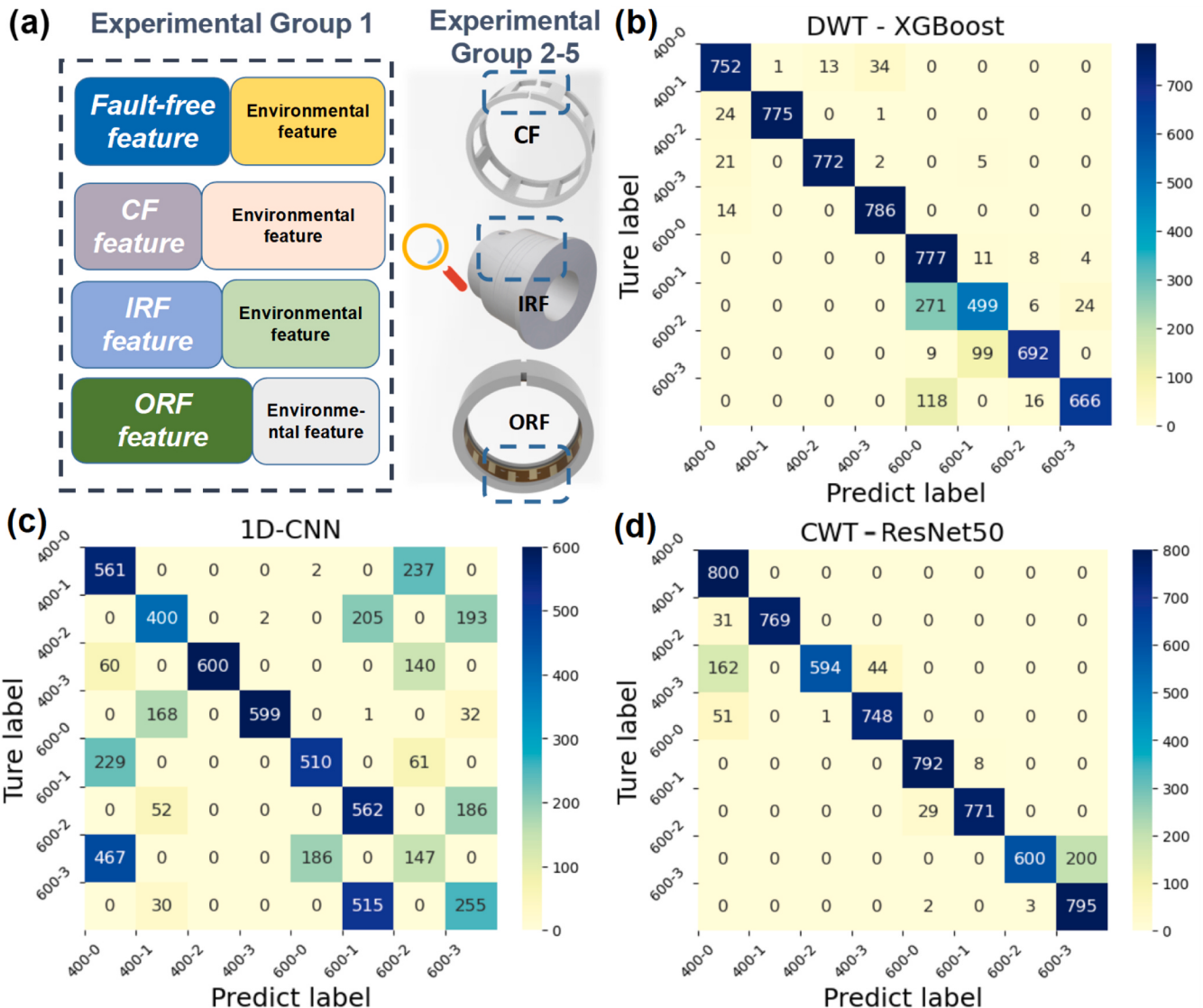


Fig. 6. Robustness study of classification methods. (a) Schematic illustration of the signal feature composition. (b) Confusion matrix of DWT-XGBoost, (c) 1D-CNN, and (d) CWT-ResNet50.

wavelet transform. Fig. 5f shows an image obtained through CWT on the output at 600 rpm. These images are then classified using the deep learning algorithm ResNet50. The batch size is set to 4, while the learning rate is set to 0.00001. After 25 epochs of training, the classification accuracy can reach 100%.

A general data partitioning method leads to the same distribution of training set and test set [39]. The outputs of various categories were measured by replacing artificially made faulty parts of the TCRB. Since triboelectric signals are susceptible to environmental factors such as humidity and temperature [37], the experimental environmental conditions cannot be completely consistent. Therefore, we believe that the feature of measured signals includes faulty part and environmental part, as illustrated in Fig. 6a. The high diagnostic accuracy of these four classification methods mentioned above in experimental group 1 may be attributed to the introduction of environmental features during faulty parts replacement rather than grasp fault features. To further corroborate the robustness of these classification methods to slight environmental interference, a new experiment based data partitioning method is proposed. The specific steps are as follows. Four additional groups of experiments were conducted, named experimental group 2–5, with the same data structure as experimental group 1. Each group of experiments was conducted over a specific period of time, and the output of various categories was obtained by replacing faulty parts. Thus, the environmental features of the samples in the same category from different experimental groups vary. If the model trained in experimental group 1 has a high recognition rate of the samples from experimental group 2–5, it indicates that this model is able to identify fault features. Herein, four identical classification methods are utilized once again to test their robustness to slight environmental interference. At this time, experimental group 1 is regarded as the training set and the remaining experimental groups as the test set.

First, for the PCA-XGBoost method, the classification accuracy is only 34.05% this time when employing the first 100 principal components, showing a significant decline. It implies that this method identifies environmental features rather than fault features, indicating that the PCA-XGBoost method is fragile and inappropriate for fault diagnosis of the TCRB. The corresponding confusion matrix is presented in Fig. S5. Then, we test the recognition performance of the DWT-XGBoost method, and the classification accuracy can reach 89.36%, confirming its robustness for fault diagnosis of the TCRB. The corresponding confusion matrix is shown in Fig. 6b. Furthermore, the influences of extracted features, wavelet basis and classifier on the diagnostic results are investigated. As illustrated in Fig. 5d (ii), three combinations of various wavelet bases and extracted features are tested using different classifiers. The classification accuracy result is illustrated in Fig. S6. It can be found that the wavelet basis and the number of extracted features have an impact on the classification accuracy for the DWT method. However, selecting the appropriate wavelet basis and extracted features prior to verification is difficult. Compared with support vector machine (SVM), XGBoost exhibits better classification performance here. Next, the 1D-CNN method is implemented, and the classification accuracy obtained is 56.78%, indicating that its robustness performance is average. Fig. 6c presents the corresponding confusion matrix. Lastly, the model trained by the CWT-ResNet50 method through experimental group 1 is used to classify the samples from experimental group 2–5, achieving a classification accuracy of 91.7%. Compared to the other three classification methods, the CWT-ResNet50 method demonstrates the highest classification performance, confirming its excellent robustness in the self-diagnosing of the TCRB. The corresponding confusion matrix is illustrated in Fig. 6d.

Overall, the diagnostic robustness of the distinct methods varies considerably. By comparing four classification methods, it is found that DWT-XGBoost and CWT-ResNet50 methods exhibit acceptable performance in classification accuracy and robustness. The performances of all classification methods on the data processed through the experiment based data partitioning method decrease, which is caused by the

operation of replacing the faulty part. Since triboelectric signals are sensitive to slight environmental change, there will be differences in the distribution between the training set (experimental group 1) and the test set (experimental group 2–5). Some classification methods, such as PCA-XGBoost, can achieve acceptable diagnostic accuracy under the condition that training and test sets are drawn from the same distribution (experimental group 1). However, the introduction of slight environmental changes leads to a significant decrease in diagnostic accuracy. This is unacceptable, especially in the actual operating environment, where the interference can become more severe. Therefore, attention should be paid to the robustness of the trained model for the application of the TCRB in fault diagnosis. Next, the robustness of the classification method in the face of obvious environmental changes needs further research.

4. Conclusion

In conclusion, a novel TENG-based cylindrical roller smart bearing is proposed. Given the mechanical properties and the output performance of the device, PEEK rollers and nylon film are selected to fabricate the TCRB. The reliability of the TCRB is demonstrated by 600,000 cycles of operation. A maximum output power of 38.4 μW is achieved at 600 rpm when the external load is approximately 30 $\text{M}\Omega$. The energy collected by the capacitor is capable of driving the temperature sensor. Through fast Fourier transform of the output signal, combined with the motion relationship formula of the bearing parts, the TCRB can realize the real-time speed sensing function with an error of less than 2%. Moreover, the electric output of the TCRB can be used as a signal to diagnose typical bearing faults. Four distinct classification methods are employed, and their classification accuracy and robustness to slight environmental interference are discussed. The CWT-ResNet50 method exhibits the best classification performance, achieving an accuracy rate of 100% on the test data with consistent distribution, and 91.7% on the test data with slightly different distribution. The capabilities of the present TCRB in self-powering, self-sensing, and self-diagnosing have been well demonstrated, thus providing a promising approach for the development of smart bearings.

CRediT authorship contribution statement

Yida Xin: Conceptualization, Methodology, Software, Writing - original draft; **Taili Du:** Methodology, Writing - review & editing, Funding acquisition; **Ting Liu:** Software; **Peiting Sun:** Supervision; **Meixian Zhu:** Validation; **Lin Zheng:** Visualization; **Haiying Du:** Methodology; **Yongjiu Zou:** Validation; **Minyi Xu:** Supervision, Writing-review & editing, Funding acquisition.

Declaration of Competing Interest

We declare that we have no financial and personal relationships with other people or organizations that can inappropriately influence our work, there is no professional or other personal interest of any nature or kind in any product, service and/or company that could be construed as influencing the position presented in, or the review of, the manuscript entitled.

Data availability

Data will be made available on request.

Acknowledgement

The work is supported by the National Natural Science Foundation of China (Grant Nos. 52101345, 52101400), Scientific Research Fund of the Educational Department of Liaoning Province (Grant No. LJKZ0055), Dalian Outstanding Young Scientific and Technological

Talents Project (2021RJ11), the Open Fund of National Center for International Research of Subsea Engineering Technology and Equipment (No. 3132023354).

Appendix A. Supporting information

Supplementary data associated with this article can be found in the online version at [doi:10.1016/j.sna.2023.114664](https://doi.org/10.1016/j.sna.2023.114664).

References

- [1] M. Woodard, M. Wolka, Bearing maintenance practices to ensure maximum life, Twenty-Seventh Int. Pump. Users Symp. (2011) 80–96, <https://doi.org/10.21423/R1SW6N>.
- [2] X. Chen, J. Van Hillegersberg, E. Topan, S. Smith, M. Roberts, Application of data-driven models to predictive maintenance: Bearing wear prediction at TATA steel, *Expert Syst. Appl.* 186 (2021), 115699, <https://doi.org/10.1016/j.eswa.2021.115699>.
- [3] B. Holm-Hansen, R. Gao, Smart bearing utilizing embedded sensors: design considerations, *Proc. SPIE 4th Int. Symp. Smart Struct. Mater.* 3041 (1997) 602–610, <https://doi.org/10.1117/12.275683>.
- [4] S.R. Kamel Tabbakh, R. Maarefdoust, N.C. Kyun, B. Mohd Ali, Environmental taxonomy of power scavenging techniques for autonomous self powered wireless sensors, *2010 IEEE Asia Pac. Conf. Circuits Syst.* (2010) 1031–1034, <https://doi.org/10.1109/apscas.2010.5774812>.
- [5] J. Chen, W. Zhang, H. Wang, Intelligent bearing structure and temperature field analysis based on finite element simulation for sustainable and green manufacturing, *J. Intell. Manuf.* 32 (2020) 745–756, <https://doi.org/10.1007/s10845-020-01702-x>.
- [6] B.T. Holm-Hansen, R.X. Gao, Structural design and analysis for a sensor-integrated ball bearing, *Finite Elem. Anal. Des.* 34 (2000) 257–270, [https://doi.org/10.1016/S0168-874X\(99\)00042-6](https://doi.org/10.1016/S0168-874X(99)00042-6).
- [7] Y. Zhang, J. Cao, Development of self-powered smart bearing for health condition monitoring, *IEEE/ASME Int. Conf. Adv. Intell. Mechatron. (AIM)* (2018) 786–791, <https://doi.org/10.1109/aim.2018.8452340>.
- [8] Y. Gong, S. Wang, Z. Xie, T. Zhang, Z. Chen, W. Lin, et al., A variable reluctance based rotational electromagnetic harvester for the high-speed smart bearing, *Smart Mater. Struct.* 31 (2022), 045023, <https://doi.org/10.1088/1361-665X/ac59d9>.
- [9] Y. Zhang, J. Cao, H. Zhu, Y. Lei, Design, modeling and experimental verification of circular Halbach electromagnetic energy harvesting from bearing motion, *Energy Convers. Manag.* 180 (2019) 811–821, <https://doi.org/10.1016/j.enconman.2018.11.037>.
- [10] F.-R. Fan, Z.-Q. Tian, Z. Lin Wang, Flexible triboelectric generator, *Nano Energy* 1 (2012) 328–334, <https://doi.org/10.1016/j.nanoen.2012.01.004>.
- [11] N. Cui, L. Gu, J. Liu, S. Bai, J. Qiu, J. Fu, et al., High performance sound driven triboelectric nanogenerator for harvesting noise energy, *Nano Energy* 15 (2015) 321–328, <https://doi.org/10.1016/j.nanoen.2015.04.008>.
- [12] W. Xu, H. Zheng, Y. Liu, X. Zhou, C. Zhang, Y. Song, et al., A droplet-based electricity generator with high instantaneous power density, *Nature* 578 (2020) 392–396, <https://doi.org/10.1038/s41586-020-1985-6>.
- [13] M. Xu, T. Zhao, C. Wang, S.L. Zhang, Z. Li, X. Pan, et al., High power density tower-like triboelectric nanogenerator for harvesting arbitrary directional water wave energy, *ACS Nano* 13 (2019) 1932–1939, <https://doi.org/10.1021/acsnano.8b08274>.
- [14] H. Gu, N. Zhang, Z. Zhou, S. Ye, W. Wang, W. Xu, et al., A bulk effect liquid-solid generator with 3D electrodes for wave energy harvesting, *Nano Energy* 87 (2021), 106218, <https://doi.org/10.1016/j.nanoen.2021.106218>.
- [15] Q. Han, Z. Ding, W. Sun, X. Xu, F. Chu, Hybrid triboelectric-electromagnetic generator for self-powered wind speed and direction detection, *Sustain. Energy Technol. Assess.* 39 (2020), 100717, <https://doi.org/10.1016/j.seta.2020.100717>.
- [16] J. Chen, G. Zhu, W. Yang, Q. Jing, P. Bai, Y. Yang, et al., Harmonic-resonator-based triboelectric nanogenerator as a sustainable power source and a self-powered active vibration sensor, *Adv. Mater.* 25 (2013) 6094–6099, <https://doi.org/10.1002/adma.201302397>.
- [17] J. Chen, Z.L. Wang, Reviving vibration energy harvesting and self-powered sensing by a triboelectric nanogenerator, *Joule* 1 (2017) 480–521, <https://doi.org/10.1016/j.joule.2017.09.004>.
- [18] T. Du, X. Zuo, F. Dong, S. Li, A.E. Mtui, Y. Zou, et al., A self-powered and highly accurate vibration sensor based on bouncing-ball triboelectric nanogenerator for intelligent ship machinery monitoring, *Micro (Basel)* 12 (2021) 218, <https://doi.org/10.3390/mi12020218>.
- [19] H. He, J. Guo, B. Illés, A. Géczy, B. Istók, V. Hliva, et al., Monitoring multi-respiratory indices via a smart nanofibrous mask filter based on a triboelectric nanogenerator, *Nano Energy* 89 (2021), 106418, <https://doi.org/10.1016/j.nanoen.2021.106418>.
- [20] P. Xu, X. Wang, S. Wang, T. Chen, J. Liu, J. Zheng, et al., A triboelectric-based artificial whisker for reactive obstacle avoidance and local mapping, *Research* 2021 (2021), <https://doi.org/10.34133/2021/9864967>.
- [21] K.Y. Lee, H.J. Yoon, T. Jiang, X. Wen, W. Seung, S.W. Kim, et al., Fully packaged self-powered triboelectric pressure sensor using hemispheres-array, *Adv. Energy Mater.* 6 (2016), 1502566, <https://doi.org/10.1002/aenm.201502566>.
- [22] P.K. Yang, Z.H. Lin, K.C. Pradel, L. Lin, X. Li, X. Wen, et al., Paper-based origami triboelectric nanogenerators and self-powered pressure sensors, *ACS Nano* 9 (2015) 901–907, <https://doi.org/10.1021/nn506631t>.
- [23] B. Zhang, L. Zhang, W. Deng, L. Jin, F. Chun, H. Pan, et al., Self-powered acceleration sensor based on liquid metal triboelectric nanogenerator for vibration monitoring, *ACS Nano* 11 (2017) 7440–7446, <https://doi.org/10.1021/acsnano.7b03818>.
- [24] C. Liu, Y. Wang, N. Zhang, X. Yang, Z. Wang, L. Zhao, et al., A self-powered and high sensitivity acceleration sensor with V-Q-a model based on triboelectric nanogenerators (TENGs), *Nano Energy* 67 (2020), <https://doi.org/10.1016/j.nanoen.2019.104228>.
- [25] W. Li, G. Liu, D. Jiang, C. Wang, W. Li, T. Guo, et al., Interdigitated electrode-based triboelectric sliding sensor for security monitoring, *Adv. Mater. Technol.* 3 (2018), 1800189, <https://doi.org/10.1002/admt.201800189>.
- [26] T. Bu, T. Xiao, Z. Yang, G. Liu, X. Fu, J. Nie, et al., Stretchable triboelectric-photonics smart skin for tactile and gesture sensing, *Adv. Mater.* 30 (2018), 1800066, <https://doi.org/10.1002/adma.201800066>.
- [27] T. Chen, Q. Shi, M. Zhu, T. He, L. Sun, L. Yang, et al., Triboelectric self-powered wearable flexible patch as 3D motion control interface for robotic manipulator, *ACS Nano* 12 (2018) 11561–11571, <https://doi.org/10.1021/acsnano.8b06747>.
- [28] X.S. Meng, H.Y. Li, G. Zhu, Z.L. Wang, Fully enclosed bearing-structured self-powered rotation sensor based on electrification at rolling interfaces for multi-tasking motion measurement, *Nano Energy* 12 (2015) 606–611, <https://doi.org/10.1016/j.nanoen.2015.01.015>.
- [29] Z. Xie, Y. Wang, R. Wu, J. Yin, D. Yu, J. Liu, et al., A high-speed and long-life triboelectric sensor with charge supplement for monitoring the speed and skidding of rolling bearing, *Nano Energy* 92 (2022), 106747, <https://doi.org/10.1016/j.nanoen.2021.106747>.
- [30] Z. Jiang, S. Gao, Y. Kong, P. Pennacchi, F. Chu, Q. Han, Ultra-compact triboelectric bearing based on a ribbon cage with applications for fault diagnosis of rotating machinery, *Nano Energy* 99 (2022), 107263, <https://doi.org/10.1016/j.nanoen.2022.107263>.
- [31] S. Gao, Q. Han, X. Zhang, P. Pennacchi, F. Chu, Ultra-high-speed hybrid ceramic triboelectric bearing with real-time dynamic instability monitoring, *Nano Energy* 103 (2022), 107759, <https://doi.org/10.1016/j.nanoen.2022.107759>.
- [32] Q. Han, Z. Ding, Z. Qin, T. Wang, X. Xu, F. Chu, A triboelectric rolling ball bearing with self-powering and self-sensing capabilities, *Nano Energy* 67 (2020), 104277, <https://doi.org/10.1016/j.nanoen.2019.104277>.
- [33] T. Du, F. Dong, M. Zhu, Z. Xi, F. Li, Y. Zou, et al., Self-powered and robust marine exhaust gas flow sensor based on bearing type triboelectric nanogenerator, *J. Mar. Sci. Eng.* 10 (2022) 1416, <https://doi.org/10.3390/jmse10101416>.
- [34] V. Chauhan, T. Kärki, J. Varis, Review of natural fiber-reinforced engineering plastic composites, their applications in the transportation sector and processing techniques, *J. Thermoplast. Compos. Mater.* 35 (2019) 1169–1209, <https://doi.org/10.1177/0892705719889095>.
- [35] V.K. Rai, A.R. Mohanty, Bearing fault diagnosis using FFT of intrinsic mode functions in Hilbert–Huang transform, *Mech. Syst. Sig. Process.* 21 (2007) 2607–2615, <https://doi.org/10.1016/j.ymssp.2006.12.004>.
- [36] J. Cai, Y. Xiao, Time-frequency analysis method of bearing fault diagnosis based on the generalized S transformation, *J. VIBROENG* 19 (2017) 4221–4230, <https://doi.org/10.21595/jve.2017.18244>.
- [37] V. Nguyen, R. Zhu, R. Yang, Environmental effects on nanogenerators, *Nano Energy* 14 (2015) 49–61, <https://doi.org/10.1016/j.nanoen.2014.11.049>.
- [38] T. Chen, C. Guestrin, XGBoost: A scalable tree boosting system, *22Nd ACM SIGKDD Int. Conf. Knowl. Discov. Data Min.* (2016) 785–794, <https://doi.org/10.1145/2939672.2939785>.
- [39] Z. Tong, W. Li, B. Zhang, M. Zhang, Bearing fault diagnosis based on domain adaptation using transferable features under different working conditions, *Shock Vib.* 2018 (2018), 6714520, <https://doi.org/10.1155/2018/6714520>.



Yida Xin received his M.S. from Lehigh University in the U.S. in 2013. From 2016 to now, he is an engineer with College of Mechanical and Electronic Engineering, Dalian Minzu University. Currently, he is pursuing his doctor degree in Dalian Maritime University, China. His current research interests include triboelectric nanogenerator and fault diagnosis of bearings.



Taili Du has been with Dalian Maritime University where he is currently an Associate Professor since 2010. He received his B.S. and M.S. from Dalian Maritime University in China in 2008 and 2010, and he is as a doctoral candidate in Marine Engineering College, Dalian Maritime University. His current research work focuses on vibration energy harvesting and self-powered vibration sensor based on Triboelectric Nanogenerator.



Lin Zheng received the Ph.D. degree from the University of Huddersfield, U.K., in 2014. From 2018 to now, she is an associate professor in the College of Mechanical and Electronic Engineering, Dalian Minzu University. Her current research is mainly focused on the fault diagnosis and condition monitoring of mechanical and electrical system, mechanical fault feature extraction and pattern recognition research.



Ting Liu received his Ph.D. degree from Dalian Maritime University in 2017. Now he is a lecturer in Dalian Minzu University. His current research is mainly focused on the areas of intelligent monitoring and predictive warning of mechanical system operation status, nonlinear vibration status monitoring and predictive warning of friction and wear, triboelectric nanogenerator, etc.



Haiying Du is a professor in the College of Mechanical and Electronic Engineering, Dalian Minzu University, China. She received his Ph.D. from the School of Electronic Science and Technology of Dalian University of Technology in 2014. Her current scientific interest is chemical sensors and detection technique.



Peiting Sun received the Ph.D. degree in naval architecture and marine engineering from the Technical University Berlin, Germany, in 1993. From 1996 to now, he is a professor with marine engineering college, Dalian Maritime University. He is also a member of Naval Architecture and Ocean Engineering Discipline Appraisal Group of the State Council's Academic Degree Committee, an expert in the field of modern transportation technology in the National 863 Program, a member of the Expert Committee of the Ministry of Transport. His research interests include green ship and intelligent ship operation and maintenance technologies.



Yongjiu Zou is an assistant professor at College of Marine Engineering, Dalian Maritime University. He received his B.S. and M.S. in marine engineering both from Dalian Maritime University in 2012 and 2014, respectively. His research focuses on triboelectric nanogenerators for energy harvesting and self-powered sensors.



Meixian Zhu received his B.S. in 2019. Currently, he is a postgraduate student in Marine Engineering College, Dalian Maritime University. His current research work focuses on triboelectric nanogenerator and artificial intelligence algorithm.



Minyi Xu received his Ph.D. degree from Peking University in 2012. During 2016–2017, he joined Professor Zhong Lin Wang's group at Georgia Institute of Technology. Now he is a Professor in the Marine Engineering College, Dalian Maritime University. His current research is mainly focused on the areas of blue energy, self-powered systems, triboelectric nanogenerators and its practical applications in smart ship and ocean.